Performance evaluation of radar and satellite rainfalls for Typhoon Morakot over Taiwan: Are remote-sensing products ready for gauge denial scenario of extreme events?

Sheng Chen [a,b,c], Yang Hong [a,b,c,*], Qing Cao [b,c], Pierre-Emmanuel Kirstetter [b,c,d], Jonathan J. Gourley [d], Youcun Qi [d], Jian Zhang [d], Ken Howard [d], Junjun Hu [b,c,e], Jun Wang [f]

[a] Department of Civil Engineering and Environmental Science, University of Oklahoma, Norman, OK 73072, United States
[b] Hydrometeorology and Remote Sensing Laboratory, University of Oklahoma, Norman, OK 73072, United States
[c] Advanced Radar Research Center, University of Oklahoma, Norman, OK 73072, United States
[d] National Oceanic and Atmospheric Administration/National Severe Storms Laboratory, Norman, OK 73072, United States
[e] School of Computer Science, University of Oklahoma, Norman, OK 73072, United States
[f] Nansen-Zhu International Research Centre, Institute of Atmospheric Physics, Chinese Academy of Sciences, Beijing 100029, China

ARTICLE INFO

SUMMARY

This study evaluated rainfall estimates from ground radar network and four satellite algorithms with a relatively dense rain gauge network over Taiwan Island for the 2009 extreme Typhoon Morakot at various spatiotemporal scales (from 0.04° to 0.25° and hourly to event total accumulation). The results show that all the remote-sensing products underestimate the rainfall as compared to the rain gauge measurements, in an order of radar (−18%), 3B42RT (−19%), PERSIANN-CCS (28%), 3B42V6 (−36%), and CMORPH (−61%). The ground radar estimates are also most correlated with gauge measurements, having a correlation coefficient (CC) of 0.81 (0.82) at 0.04° (0.25°) spatial resolution. For satellite products, CMORPH has the best spatial correlation (0.70) but largely underestimates the total rainfall accumulation. Compared to microwave ingested algorithms, the IR-dominant algorithms provide a better estimation of the total rainfall accumulation but poorly resolve the temporal evolution of the warm cloud typhoon, especially for a large overestimation at the early storm stage. This study suggests that the best performance comes from the ground radar estimates that could be used as an alternative in case of the gauge denial. However, the current satellite rainfall products still have limitations in terms of resolution and accuracy, especially for this type of extreme typhoon.

© 2012 Elsevier B.V. All rights reserved.

1. Introduction

Morakot is the deadliest typhoon that has hit Taiwan in its recorded history. It formed on 2 August 2009 as an unnamed tropical depression in its early stage and landed on Hualien, Taiwan at 23:45 PM on 7 August 2009. Roughly 24 h later, the storm moved back into the Taiwan Strait and weakened to be a severe tropical storm before landing mainland China on 9 August 2009. The typhoon eventually dissipated on 11 August 2009. During its span in Taiwan, Morakot brought about catastrophic impacts, including 461 deaths, 192 missing, and roughly 3.3 billion USD in property damages. The storm produced copious amounts of rainfall with a maximum 2777 mm, surpassing the previous record of 1736 mm

set by Typhoon Herb in 1996.[1] The extreme amount of rainfall triggered severe flooding and enormous mudslides in southern Taiwan, caused so called gauge denial situations where ground rain gauges either washed away or damaged. Alternatively, remote sensing platforms such as ground radar and satellites can provide quantitative precipitation estimation (QPE) in poorly gauged or gauge-denied regions.

Today, the satellite-based QPE products have been capturing more attentions to their global coverage and virtually uninterrupted temporal continuity. The popular satellite-based QPE products include the infrared (IR)-dominated precipitation estimation from remotely sensed information using artificial neural networks (Sorooshian et al., 2000) and later the PERSIANN-Cloud Classification System (PERSIANN-CSS, (Hong et al., 2004), the microwave-dominated CMORPH product (Joyce et al., 2004), the TRMM Multi-satellite Precipitation Analysis (TMPA) 3B42RT and 3B42V6

1 http://en.wikipedia.org/wiki/Typhoon_Morakot.

products (Huffman et al., 2007), among many others (Turk and Miller, 2005). Those state-of-the-art remote sensing QPE products have been widely used in the applications of climate change, hydrologic modeling, and hazards monitoring (Change, 2007; Creutin and Borga, 2003; Diaz et al., 2001; Hong et al., 2007a,b; Liang, 1994; Ogden et al., 2000; Vicente et al., 1998; Wang et al., 2011; Zhao, 1992). In order to understand the performance of these remote sensing QPE products, efforts have been put into revealing the error characteristics of these products (Amitai et al., 2012; Gourley et al., 2010, 2011; Habib et al., 2009; Kirstetter et al., 2010, 2011, 2012). Results show that they have different limitations in providing accurate QPE at hydrologic relevant scale, especially for extreme typhoon events such as Morakot. Particularly as a mountainous island, Taiwan poses a unique challenge to remote sensing rainfall retrieval.

This study aimed to compare rainfall estimates from ground radars and four satellite algorithms with a relatively dense rain gauge network over Taiwan Island for the 2009 extreme Morakot Typhoon at various spatiotemporal scales (from 0.04° to 0.25° and hourly to event total accumulation). The primary objective is to evaluate the performance of remote-sensing rainfall estimation through using the rain gauge observations as a benchmark. The secondary objective is to assess if the current remote sensing rainfall products can be a good substitute of the conventional gauge measurements of rainfall, which might be unavailable due to natural or anthropogenic reasons, particularly in such an extreme typhoon (Harris and Hossain, 2008). The paper is organized as follows. Section 2 describes the study region and available rainfall products to be evaluated for Typhoon Morakot. Section 3 provides an analysis of spatial characteristics and error quantification for the rainfall brought by Typhoon Morakot to Taiwan Island from 00:00 AM on 7 August 2009 to 23:00 PM on 8 August 2009. The total rainfall accumulation, the mean hourly rainfall, and the hourly-accumulated rainfall are evaluated as a function of rainfall intensity. Section 4 gives a summary of analysis results and draws the conclusion.

2. Study region and data

2.1. Study region

The study region, Taiwan Island, is located at the east of Taiwan Strait and close to the southeastern coast of Chinese mainland, spanning from 21°53′N to 25°18′N in latitude and from 120°08′E to 122°01′E in longitude. As shown in Fig. 1a, the Tropic of Cancer (23.5°N) divides the island into two climate regions, the tropical monsoon region in the south and the subtropical monsoon region in the north.

Eastern Taiwan is mostly mountainous while the western normally has gently sloping plains. High temperature and humidity, massive rainfall and tropical cyclones are weather features of summer in Taiwan Island. Its latitude and topography, ocean current and monsoon are major factors contributing to the precipitation in this island.[2] Because Taiwan is located in the path of typhoons in northwest Pacific, there are on average 3.5 typhoons striking Taiwan every year. The typhoons bring heavy rainfall and cause serious natural disasters such as flood and landslide. As to Morakot, heavy precipitation has triggered the debris flow disaster and severely damaged the Shiaolin Village of Kaosiung County. The landslide and collapse that were caused by the erosion of torrential rainfall buried the whole village and resulted in more than 400 death and missing people.

2.2. Ground rainfall products

Taiwan Island has two different kinds of ground rainfall products, one from the hundreds of gauge stations and the other from the four Weather Surveillance Radar–1988 Doppler (WSR-88D) radars. The gauge-based rainfall product gives the hourly precipitation and is provided by Taiwan Weather Bureau. There are total 494 gauge stations in Taiwan and Penghu Islands. These gauges have undergone real-time manual QC in Central Weather Bureau of Taiwan. Many studies were conducted with these gauges (Chen et al., 2007; Fang et al., 2011; Hall et al., 2011). However, some gauges did not record rainfall data from 00:00 AM on 7 August 2009 to 23:00 PM on 8 August 2009 and these gauges were flagged and removed from the analysis. The remaining 278 gauges located in Taiwan Island (colored circular points in Fig. 1a) provided automated reports of rainfall in every 10 min, based on which the 1-h rainfall was derived for the analysis. The gauge measurements were assumed to provide the ground truth for the evaluation of remote-sensing rainfall products in the rest of this paper.

The radar-based QPE product is derived from the observations of four WSR-88D radars (green triangles in Fig. 1a) with a 10-min interval and a 0.01° spatial resolution. The multi-radar mosaic and retrieval algorithms are based on the US National Mosaic QPE system developed by the National Severe Storms Laboratory of National Oceanic and Atmospheric Administration (Qi et al., 2012; Zhang et al., 2011, 2004), which provides very high temporal and spatial resolution (e.g., 5 min, 1 km) QPE product over the Continental of US. For the convenience of comparison of satellite products, the radar-based QPE product was interpolated into the analysis grid of 0.04° and 0.25° in latitude and longitude.

2.3. Satellite data

Four satellite rainfall products from three different retrieval algorithms have been evaluated in this study, namely the PERSIANN-CCS, CMORPH, and the third one TMPA including a real-time version product (3B42RT) and a gauge-corrected post-real-time research product (3B42V6).

PERSIAN-CCS, an automated system for precipitation estimation from remotely sensed information using the artificial neural network, extracts local and regional cloud features from infrared geostationary satellite imagery to estimate a finer-scale (i.e. 0.04° × 0.04°, 30 min) rainfall distribution. The system could retrieve different rainfall rates at a given brightness temperature (T_b) and detects variable rain/no-rain IR thresholds for different cloud types. There are two PERSIANN-CCS products available, namely a real-time (RT) version and a microwave-adjusted (MW) version. After benchmarking, the PERSIANN-CCS-RT algorithm converts the real-time satellite cloud images of Geostationary Satellite system (GOES) into the estimate of rainfall rate. Later the PERSIANN-CCS-MW algorithm uses microwave precipitation estimates from low earth-orbiting satellite platforms, such as TRMM and other microwave satellites to sequentially calibrate the RT products into an IR/MW combined products. The real-time data from the current version of PERSIANN-CCS are available online both at regional (http://hydis8.eng.uci.edu/CCS/) and global scales (ftp://earth.eng.uci.edu/CCS/). In this study, the real-time PERSIANN-CCS is used at aggregated hourly and 0.04° or 0.25° grid scale.

CMORPH is a technique that was developed to synergize the most desirable aspects of passive microwave (high quality) and infrared (high spatial and temporal resolution) data. As a quasi-global (60°S–60°N in longitude) high-resolution (0.1° in latitude/longitude, half-hourly) precipitation analysis technique, it uses the motion vectors derived from the half-hourly geostationary satellite IR imagery to extrapolate the passive microwave precipitation estimates. Therefore, it improves the estimation of

---

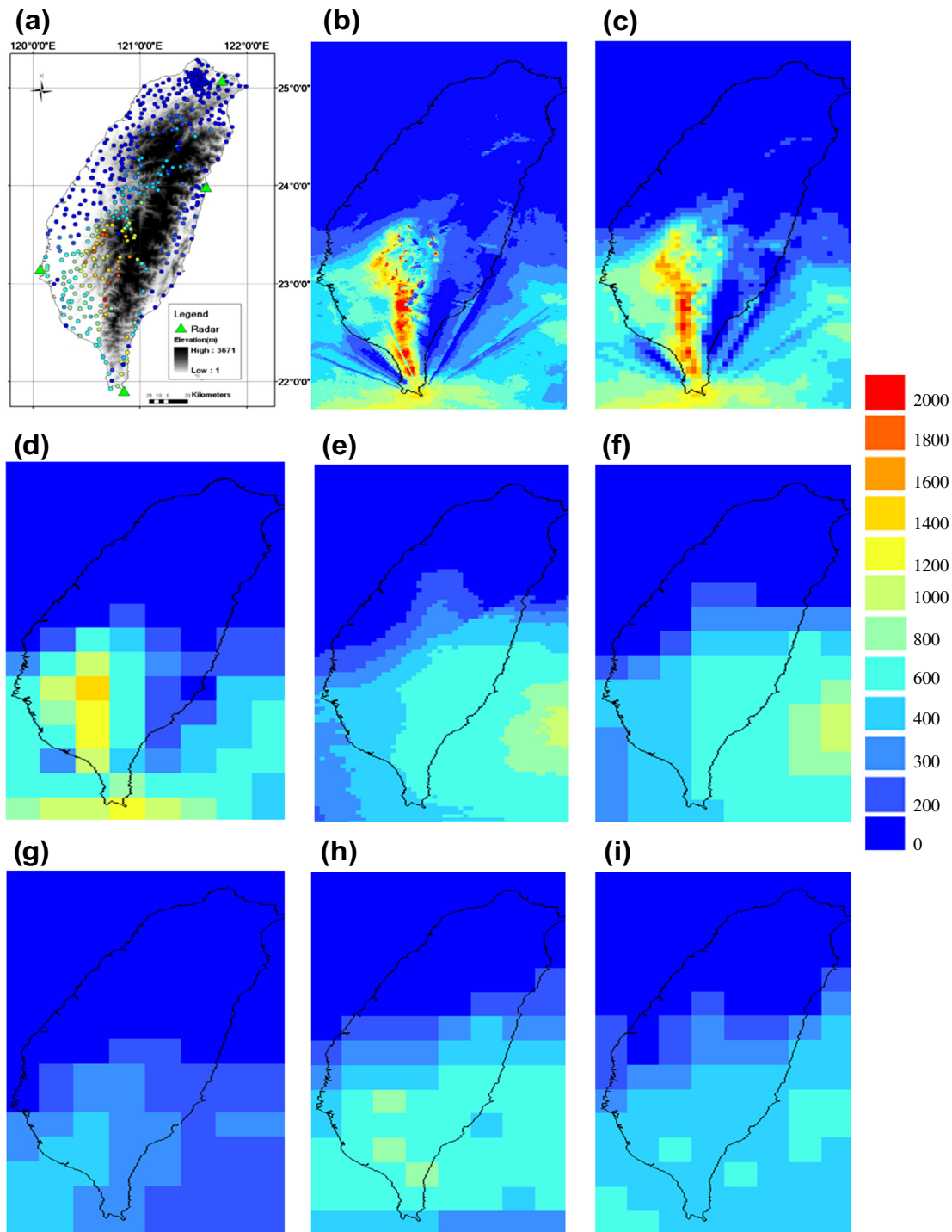[2] http://twgeog.geo.ntnu.edu.tw/english/climatology/climatology.htm.

Fig. 1. Accumulated rainfall on August 7–8, 2009 based on: (a) gauge-based product; (b)–(d) radar based products for 0.01, 0.04 and 0.25° resolutions, respectively; (e)–(f) PERSIANN-CCS products for 0.04 and 0.25° resolutions, respectively; (g) CMORPH product at 0.25°; (h) 3B42RT product 0.25°; and (i) 3B42V6 product 0.25°.

multi-hour precipitation accumulation, better than the simple averaging of available microwave-based estimates and other merging results that incorporate microwave and infrared information in the estimation (Joyce et al., 2004).

3B42RT is a nearly-real-time product and 3B42V6 is a post-real-time product. Both of them are 3B42-level products and have been provided to the research community by TMPA. 3B42RT(3B42V6) covers the region of 50°S–50°N (60°S–60°N) in latitude. The real-time product 3B42RT uses rainfall estimates from TRMM Precipitation Radar and TRMM Microwave Imager to calibrate the estimates from low-earth-orbiting passive microwave (PM) radiometers. All

these estimates are merged into a product with a 3-h interval in 3B42RT. Gaps in these analyses are filled using geosynchronous infrared data regionally calibrated to the merged microwave products. The 3B42V6 analyzes the monthly rainfall accumulation calculated from 3B42RT 3-h product and adjusts it by the monthly gauge analysis, which combines the Climate Assessment and Monitoring System (CAMS) 0.5° × 0.5° monthly gauge product and the Global Precipitation Climatology Center (GPCC) 1.0° × 1.0° monthly gauge product. The monthly ratio between the satellite-only analysis and the monthly gauge product is used to rescale the individual 3-h satellite-only analysis (Huffman et al., 2007).
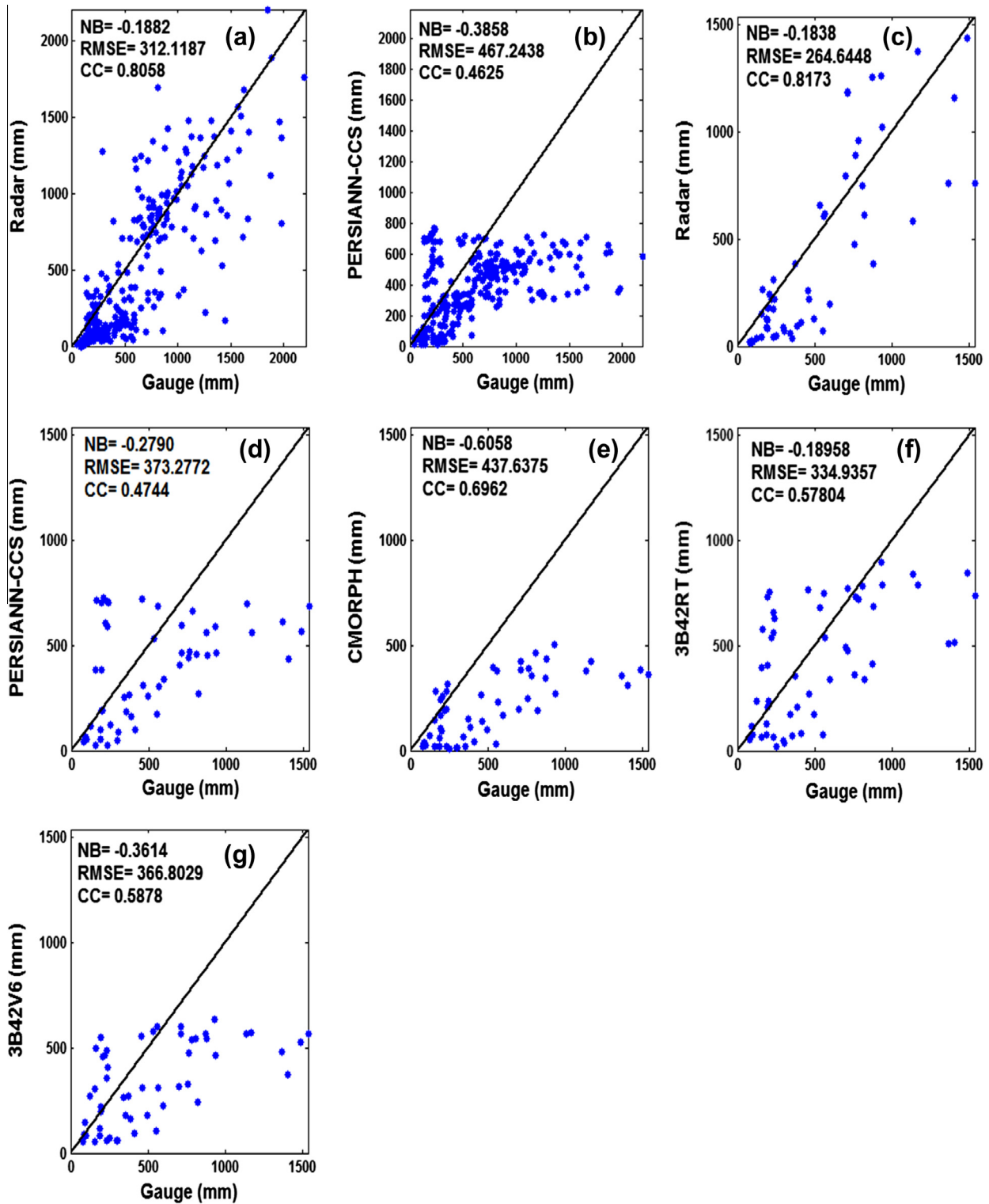
Fig. 2. Scatter plots of two-day rainfall accumulation from various sources versus gauge measurements. Bulk statistics are shown in the upper-left corner of each panel. (a) radar (0.04°); (b) PERSIANN-CCS (0.04°); (c) radar (0.25°); (d) PERSIANN-CCS (0.25°); (e) CMORPH (0.25°); (f) 3B42RT (0.25°); and (g) 3B42V6 (0.25°).

Table 1
Series CC based on 6 h-mean precipitation.

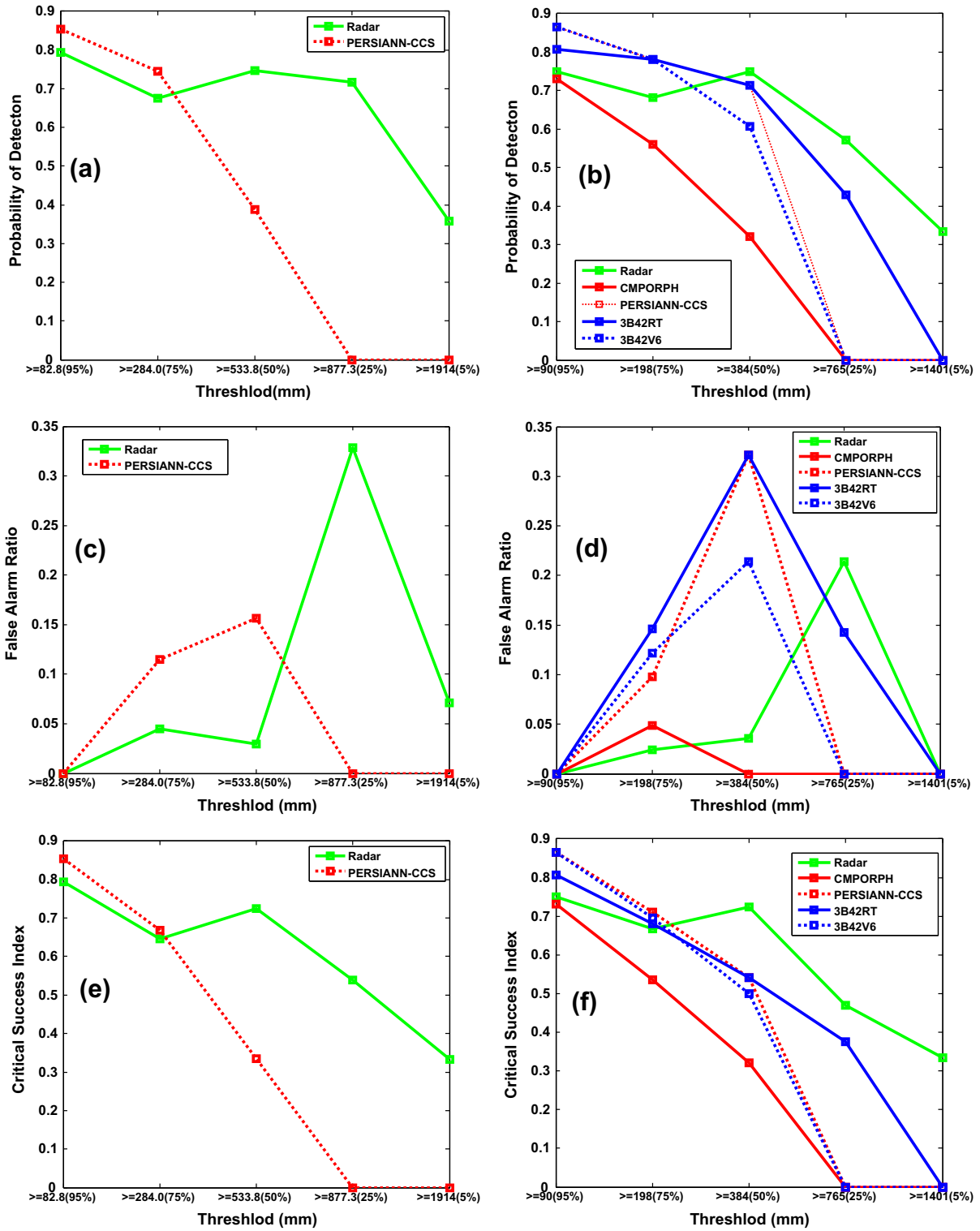| Time	0–5 h	6–11 h	12–17 hr	18–23 h	24–29 h	30–35 h	35–41 h	42–47 h
Radar	0.6225	0.6358	0.8116	0.8618	0.9066	0.8144	0.8042	0.7368
CMORPH	0.2432	0.3527	0.4599	0.8078	0.7563	0.5696	0.4953	0.5005
PERSIANN	0.0241	0.1187	0.1877	0.8142	0.6055	0.2220	0.2125	0.0625
3B42RT	−0.0331	0.1622	0.1561	0.7810	0.7919	0.4671	0.4457	0.4857
3B42V6	0.0211	0.2300	0.0287	0.5538	0.7670	0.0084	0.3060	0.3908

Fig. 3. Comparison of POD, FAR and CSI based on different rainfall thresholds. Thresholds amounts are set as 83, 284, 534, 877 and 1914 mm for the scale of 0.04° (left) and set as 90, 198, 384, 765 and 1401 mm for the scale of 0.25° (right). The thresholds are determined from 5%, 25%, 50%, 75% and 95% percentiles of the total rainfall accumulation of gauge measurements.

2.4. Evaluation indices

Normalized bias (NB), root-mean-squared error (RMSE), correlation coefficient (CC), probability of detection (POD), false alarm ratio (FAR) and critical success index (CSI) are used in this study to evaluate the performance of all the rainfall algorithms. NB, RMSE and CC are defined as follows.

$$NB = \frac{\sum(QPE - gauge)}{\sum gauge} \quad (1)$$

$$RMSE = \sqrt{\frac{\sum(QPE - gauge)^2}{N}} \quad (2)$$

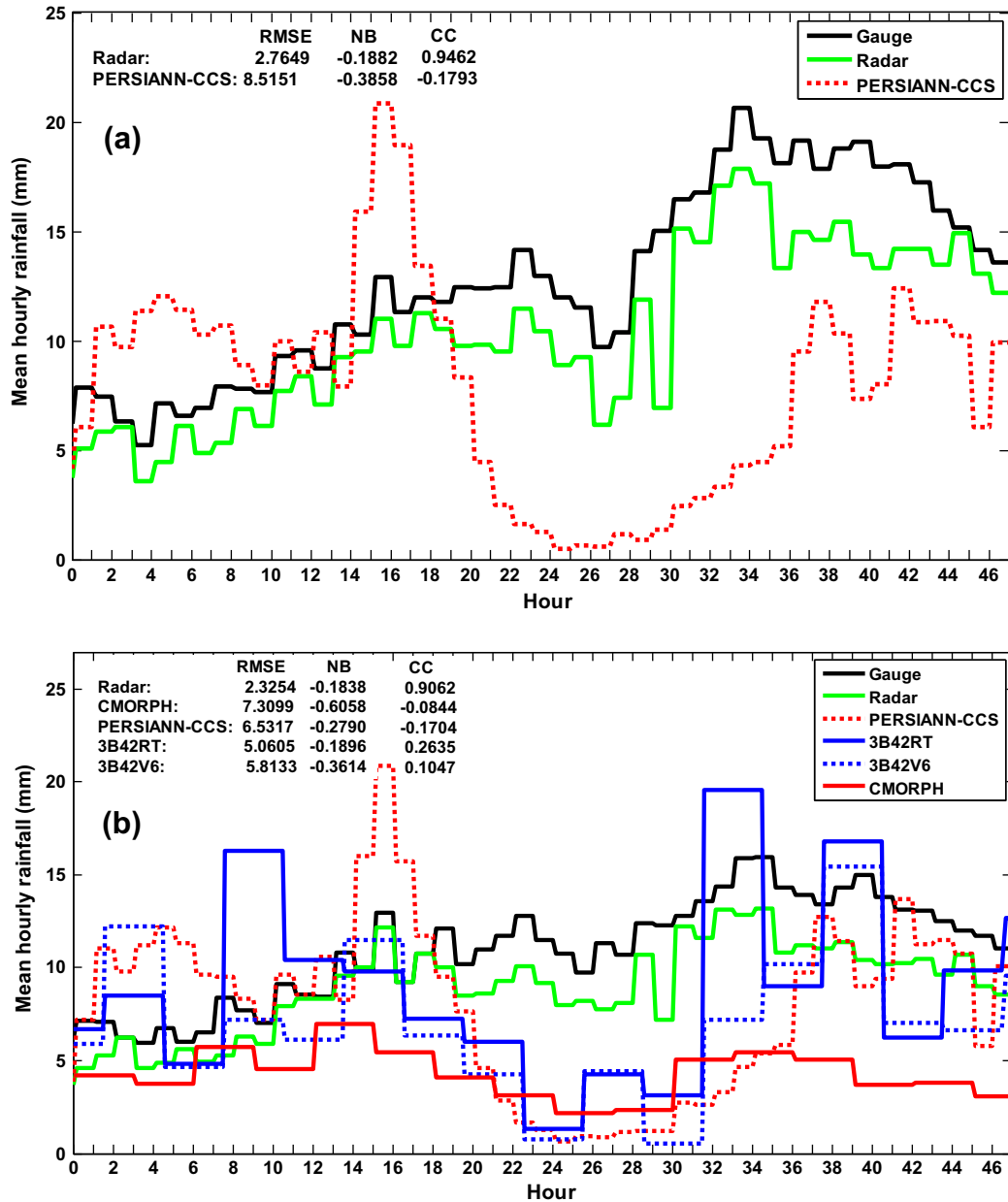**Fig. 4.** Temporal variation of mean hourly rainfall in the scale of: (a) 0.04°, and (b) 0.25°.

$$CC = \frac{Cov(QPE, gauge)}{\sigma_{QPE}\sigma_{gauge}} \qquad (3)$$

where NB and CC are dimensionless, RMSE is in mm. In Eq. (3), "Cov ()" refers to the covariance, and σ indicates the standard deviation. NB, when multiplied by 100, denotes the degree of overestimation or underestimation in percentage. All the above statistics have been computed on a pixel-by-pixel basis.

Statistics of POD, FAR and CSI have been computed using the numbers of hit (A), false alarm (B), and miss (C) in the following equations:

$$POD = \frac{A}{A+C} \qquad (4)$$

$$FAR = \frac{B}{A+B} \qquad (5)$$

$$CSI = \frac{A}{A+B+C} \qquad (6)$$

3. Analysis of rainfall products

3.1. Accumulated rainfall over Taiwan Island

Rainfall estimates from all the products have been accumulated from 00:00 AM on 7 August 2009 to 23:00 PM on 8 August 2009 to yield two-day total rainfall as shown in Fig. 1. More importantly, all of the rainfall products have shown their intense rainfall area in the southern of Taiwan Island. However, it is also worth noting that the areas with the most intense rainfall are different for these products, especially for PERSIANN-CCS and 3B42V6 products. The gauge product identified its intense rainfall area on the top and

west of the central mountain range, south of the Tropic of Cancer. The ground radar products almost have the identical intense rainfall area to the gauge product. The PERSIANN-CCS product shows intense rainfall in the east of southern Taiwan coast (Fig. 1e and f). This suggests the inherent shortage of IR technique that using IR brightness temperatures to estimate precipitation will yield a large error when the convective cloud has a higher brightness temperature than the commonly used temperature threshold (Negri

and Adler, 1993; Tuttle et al., 2008). The strong wind under the cloud might contribute to the underestimation. The CMORPH product shows the intensive rainfall in the southwestern of Taiwan Island (Fig. 1g) with a similar spatial structure to gauge and radar products except that it exhibits much less rainfall amount than other products. This might be due to: (1) the missed precipitation that forms and develops over an area outside of passive microwave overpasses mosaics; or (2) the ice areas assigned with zero rainfall
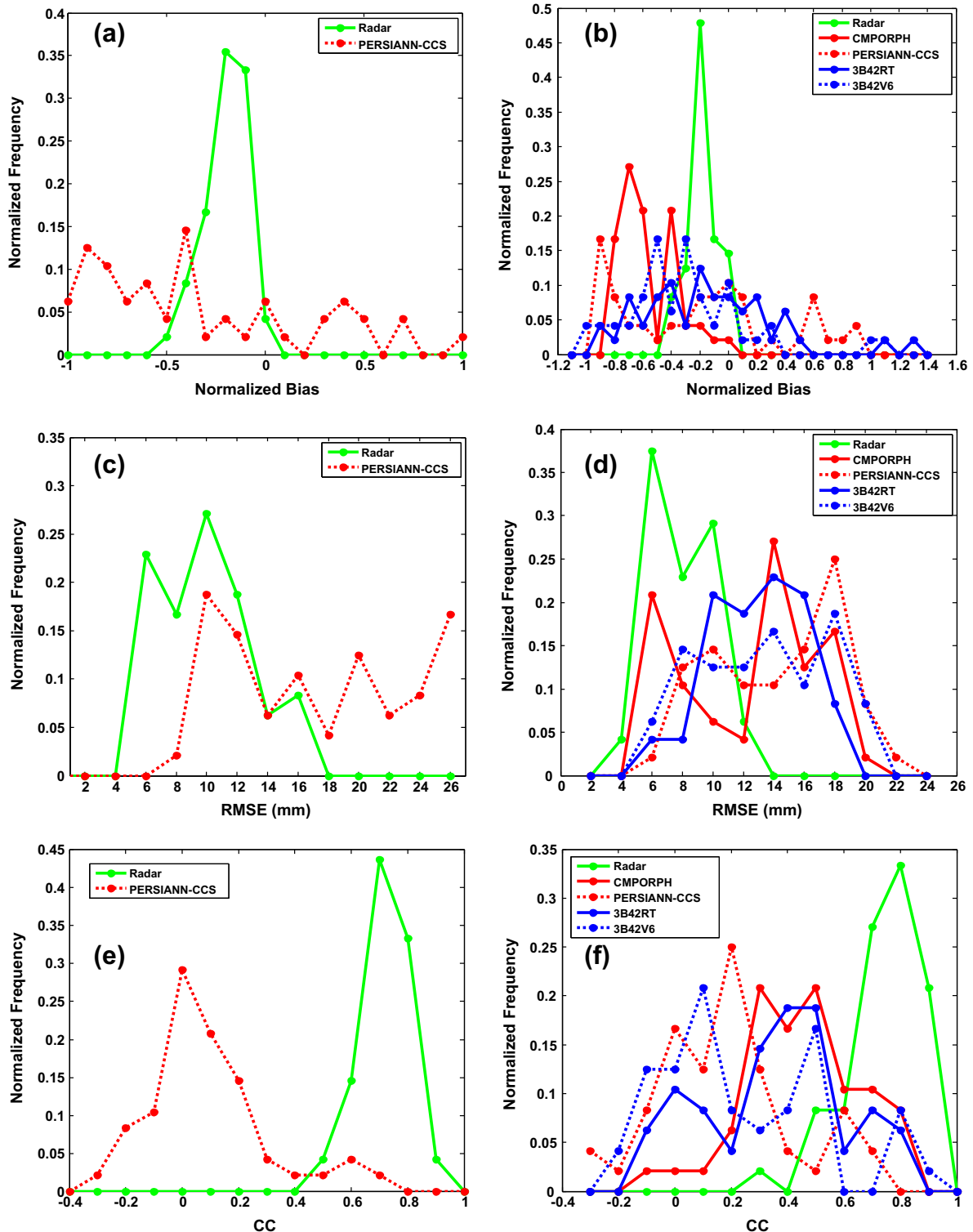

Fig. 5. Normalized occurrence frequency of NB, RMSE and CC for mean hourly rainfall in the scale of 0.04° (left column) and 0.25° (right column).

estimates by the snow screening process in the CMORPH algorithm (Joyce et al., 2004; Zhang, 2012). The performance of PERSIANN-CCS and CMORPH over the mountainous Taiwan island is consistent with the findings in Hirpa et al. (2010) and by (Zhang, 2012) over the complex terrain during heavy precipitation events. For TRMM products, 3B42RT can capture the intensive rainfall area indicated by ground radar product, but the effect of IR sensor is still there as seen in the PERSIANN-CCS product, which suggests that an limitation in the probability-matching assumption that the colder cloud top brightness temperatures correspond to higher precipitation rates for the gap-filling IR/MW histogram matched-based precipitation estimation (Huffman et al., 2007; Yong et al., 2010). With the adjustment by gauge measurements, 3B42V6 presents less heavy rainfall than 3B42RT and this may be due to the process of rescaling the 3B42RT to the monthly rain gauge data. The temporal fluctuation of precipitation might be therefore smoothed during

the typhoon event. These results are consistent with the findings by Dinku et al. (2010) over complex topography and findings by Habib et al. (2009) over the tropical-related heavy rainfall events.

For quantitative comparison of remote-sensing and gauge measurements, only the grids that cover the rain gauge site have been used. Such grid-based comparison technique was applied in many previous studies (Adler et al., 2003; Chiu et al., 2006; Chokngamwong and Chiu, 2008; Nicholson et al., 2003; Yong et al., 2010). 266 grids (57 grids) are available for the direct comparison with a $0.04° \times 0.04°$ ($0.25° \times 0.25°$) spatial resolution. Scatter plots of various rainfall products versus gauge measurements are shown in Fig. 2. These plots indicate radar has the best performance in terms of NB, RMSE and CC either in the scale of 0.04° or 0.25°. It has the highest CC (0.82), lowest NB (−0.1838, indicating rainfall underestimation by 18.38%) and RMSE (264.64 mm). Among the satellite products, 3B42RT has the least rainfall underestimation
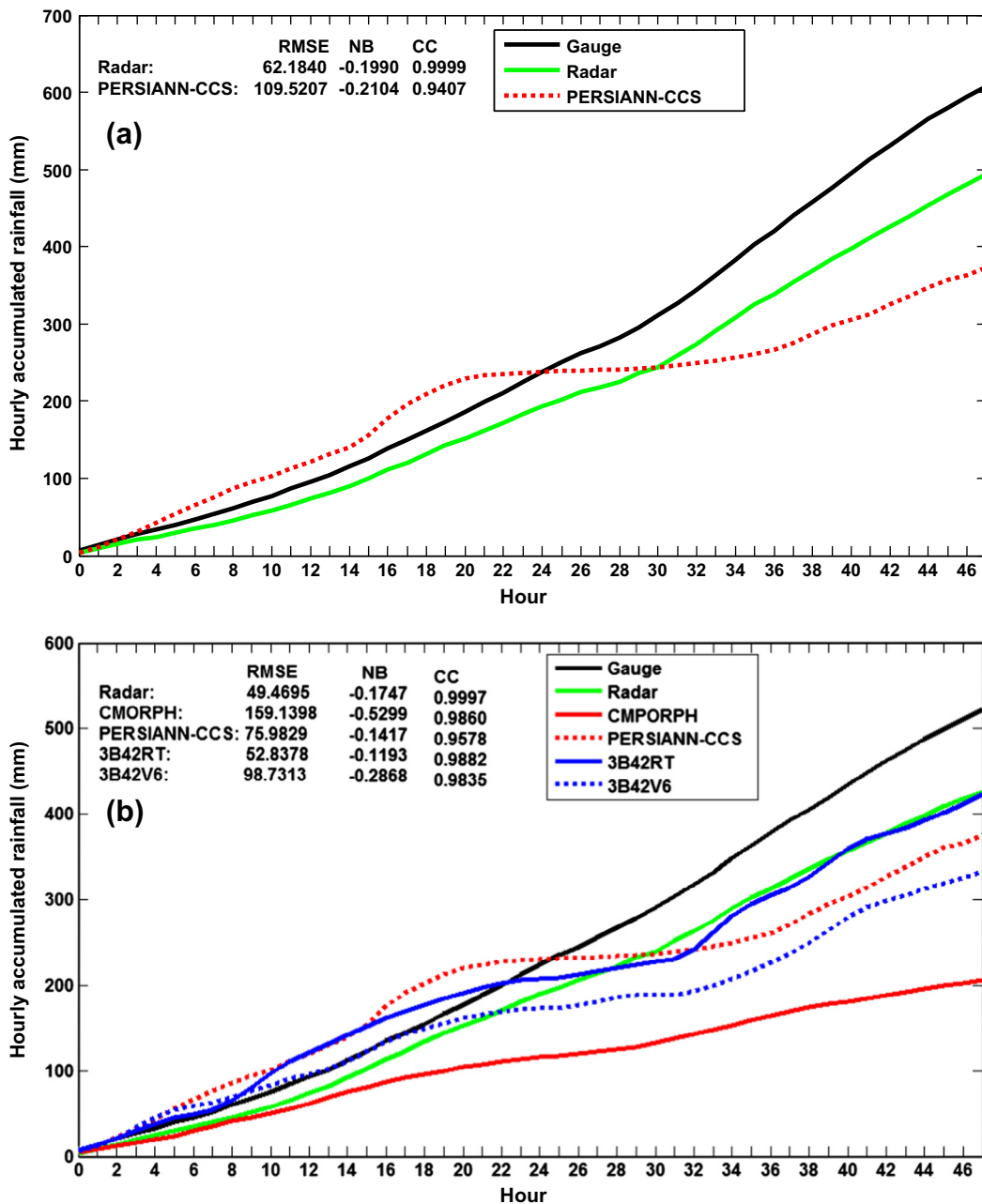

Fig. 6. Hourly accumulated rainfall in the scale of: (a) 0.04°, and (b) 0.25°.

(by 18.96%), the lowest RMSE (334.94 mm) and a moderate CC of 0.58. CMORPH has a large RMSE of 437.64 mm and a NB of −0.6058 (underestimation by 60.58%). For more details, Table 1 provides the CCs for different kinds of products based on 6-h mean precipitation. The table reveals that radar also has the highest CCs at difference time durations and CMORPH still has higher CCs than other satellite-based products. This result is consistent with the spatial distribution of rainfall accumulation shown in Fig. 1.

Fig. 3 shows the comparison of POD, FAR and CSI for different rainfall products at the scales of 0.04° and 0.25°. Radar products generally have a better POD and CSI than satellite products at all rainfall thresholds. In particular, the POD and CSI values for thresholds greater than 83 mm and 1914 mm demonstrate that the ground radar has the best ability to capture both light and heavy rainfall. Its FAR at threshold 877 mm, however, is a little higher than other thresholds. This relative high false alarm is likely caused by the non-uniform beam filling (NUBF) of precipitation signals. The enlarged radar resolution volume at a far range and the inhomogeneity of precipitation system are the major reasons. All the satellite products, except the CMOPH, have a POD greater than 0.7 at threshold 90 mm and similar POD values (0.7 < POD < 0.81) at the second and third thresholds (198 mm and 384 mm). They all have high FAR (>0.2) at the third threshold. CMORPH normally has a relatively lower FAR due to its low detection as shown in Fig. 1.

3.2. Mean hourly rainfall over Taiwan Island

Fig. 4 shows the plots of 48-h time series of mean hourly rainfall for gauge, radar and satellite products, and statistics was computed based on the hourly rainfall of various QPE products (hourly projection from 3-h time series rainfall of satellite products if necessary, e.g. the 2nd hour precipitation of 3B42RT can be computed by pulsing the result of multiplying the mean rainfall with the time stamp centered on 00:00 with 0.5 and the result of multiplying the mean rainfall with the time stamp centered on 03:00 with 0.5). The gauge observed rainfall generally increases steadily from the first day to the second day with the peak occurring at the 33rd hour. The radar-based rainfall well captures the temporal evolution of the gauge measurements, with only slight but very persistent underestimation of the whole period. The statistics show that radar has the highest CC (>0.9), smallest RMSE (<3 mm) and least underestimation (<19%) in either scale of 0.04° or 0.25°, as shown in Fig. 4. Satellite products have great fluctuations in time series data when compared to gauge measurements, with a poor match in the temporal variation of hourly rainfall. All the satellite products have a low CC (<0.3) and a large RMSE (>5 mm), with 3B42RT relatively better performance.

Fig. 5 shows the normalized occurrence frequency of NB, RMSE and CC, computed during the time span of 48 h. In consistent with Fig. 4, it clearly shows that the radar product has the best performance, with a sharp and narrow band of NB concentrating around −18% and a distinguished high CC peaked around 0.7. In contrast, satellite products show a broader occurrence distribution of NB values and a higher occurrence frequency of large RMSE (>12 mm) and low CC (<0.5). This result also explains the large fluctuation of satellite products in the hourly rainfall as shown in Fig. 4.

3.3. Rainfall accumulation

The two-day rainfall accumulations are compared in Fig. 6. Compared to satellite products, the radar product shows very similar temporal trend and also closest magnitude to the gauge observation. Among satellite products, 3B42RT and PERSIANN-CCS show closer match, indicating the IR-dominated algorithms better

captured this warm cloud typhoon. This result also echoes the spatial map of accumulated rainfall shown in Fig. 1 and the temporal variation of hourly rainfall shown in Fig. 4.

4. Summary and conclusions

The objective of this work is to quantify several popular remote-sensing QPE products in an extreme typhoon event (Morakot) in the complex topography of Taiwan. With the gauge measurements as the ground truth, QPE results based on ground radar and four satellite algorithms have been evaluated at different temporal and spatial resolutions. Results are summarized as follows:

(a) The results show that all the remote-sensing precipitation products underestimate the rainfall: radar (−18%), 3B42RT (−19%), PERSIANN-CCS (−28%), 3B42V6 (−36%), and CMORPH (−61%).

(b) Compared to satellite algorithms, ground radar QPE has the best performance and captures the temporal variation of the 48-h rainfall very well. It is highly correlated with the gauge measurement (CC > 0.8), with the lowest RMSE and NB in the scatterplots of total rainfall accumulation (Fig. 3a and c), hourly rainfall and cumulative hourly time series (Figs. 5 and 6).

(c) Among satellite algorithms, CMORPH performs better than others in terms of spatial pattern of rainfall distribution, with a fairly good CC (0.70) for two-day rainfall accumulation. However, it has the largest underestimation of this tropical warming cloud precipitation system. On the other hand, the IR-dominated algorithms (e.g. PERSIANN-CCS) provide a better estimation of total rainfall accumulation but a worse spatial and temporal correlation, particularly overestimation at the early stage but underestimation at later stage of this typhoon event.

This study suggests that the best performance comes from the ground radar network mosaicked estimates that could be used as an alternative in cases of the ground gauge denial situations. All satellite-based QPE products demonstrated poor performance in heavy rainfall events, similar results can be found in studies of Dinku et al. (2010), Habib et al. (2009), and Zhang (2012). According to the aforementioned analysis, all these products tend to have limitations in terms of resolution and accuracy, especially for this type of extreme typhoon. It is anticipated that the 2014 to-be-lunched Global Precipitation Measuring (GPM) mission, an international satellite constellation, with the dual-frequency radar capacity and better spatiotemporal coverage, would further improve extreme rainfall estimation for small-scale hydrometeorological applications such as flood and landslide.

References

Adler, R.F. et al., 2003. The version-2 global precipitation climatology project (GPCP) monthly precipitation analysis (1979-present). J. Hydrometeorol. 4 (6), 1147–1167.

Amitai, E., Petersen, W., Llort, X., Vasiloff, S., 2012. Multiplatform comparisons of rain intensity for extreme precipitation events. Geosci. Remote Sens. IEEE Trans. 50 (3), 675–686.

Change, I.P.O.C., 2007. Climate Change 2007: The Physical Science Basis. Agenda, 6, 07.

Chen, C.S., Chen, Y.L., Liu, C.L., Lin, P.L., Chen, W.C., 2007. Statistics of heavy rainfall occurrences in Taiwan. Weather Forecasting 22 (5), 981–1002.

Chiu, L.S. et al., 2006. Comparison of TRMM and water district rain rates over New Mexico. Adv. Atmos. Sci. 23 (1), 1–13.

Chokngamwong, R., Chiu, L.S., 2008. Thailand daily rainfall and comparison with TRMM products. J. Hydrometeorol. 9 (2), 256–266.

Creutin, J.D., Borga, M., 2003. Radar hydrology modifies the monitoring of flash-flood hazard. Hydrol. Process. 17 (7), 1453–1456.

Diaz, H.F., Hoerling, M.P., Eischeid, J.K., 2001. ENSO variability, teleconnections and climate change. Int. J. Climatol. 21 (15), 1845–1862.

Dinku, T., Connor, S.J., Ceccato, P., 2010. Comparison of CMORPH and TRMM-3B42 over Mountainous Regions of Africa and South America. Springer-Verlag, New York.

Fang, X., Kuo, Y.H., Wang, A., 2011. The impacts of Taiwan topography on the predictability of typhoon Morakot's record-breaking rainfall: a high-resolution ensemble simulation. Weather Forecasting 26 (5), 613–633.

Gourley, J.J., Hong, Y., Flamig, Z.L., Li, L., Wang, J., 2010. Intercomparison of rainfall estimates from radar, satellite, gauge, and combinations for a season of record rainfall. J. Appl. Meteorol. Climatol. 49 (3), 437–452.

Gourley, J.J. et al., 2011. Hydrologic evaluation of rainfall estimates from radar, satellite, gauge, and combinations on Ft. Cobb basin, Oklahoma. J. Hydrometeorol..

Habib, E., Henschke, A., Adler, R.F., 2009. Evaluation of TMPA satellite-based research and real-time rainfall estimates during six tropical-related heavy rainfall events over Louisiana, USA. Atmos. Res. 94 (3), 373–388.

Hall, J.D., Xue, M., Ran, L., Leslie, L.M., 2011. High Resolution Modeling of Typhoon Morakot (2009): Vortex Rossby Waves and Their Role in Extreme Precipitation over Taiwan.

Harris, A., Hossain, F., 2008. Investigating the optimal configuration of conceptual hydrologic models for satellite-rainfall-based flood prediction. Geosci. Remote Sens. Lett. IEEE 5 (3), 532–536.

Hirpa, F.A., Gebremichael, M., Hopson, T., 2010. Evaluation of high-resolution satellite precipitation products over very complex terrain in Ethiopia. J. Appl. Meteorol. Climatol. 49 (5), 1044–1051.

Hong, Y., Hsu, K.L., Sooroshian, S., Gao, X., 2004. Precipitation estimation from remotely sensed imagery using an artificial neural network cloud classification system. J. Appl. Meteorol. 43 (12), 1834–1853.

Hong, Y., Adler, R.F., Huffman, G., 2007a. An experimental global prediction system for rainfall-triggered landslides using satellite remote sensing and geospatial datasets. Geosci. Remote Sens. IEEE Trans. 45 (6), 1671–1680.

Hong, Y., Adler, R.F., Negri, A., Huffman, G.J., 2007b. Flood and landslide applications of near real-time satellite rainfall products. Nat. Hazards 43 (2), 285–294.

Huffman, G.J. et al., 2007. The TRMM multisatellite precipitation analysis (TMPA): quasi-global, multiyear, combined-sensor precipitation estimates at fine scales. J. Hydrometeorol. 8 (1), 38–55.

Joyce, R.J., Janowiak, J.E., Arkin, P.A., Xie, P., 2004. CMORPH: A method that produces global precipitation estimates from passive microwave and infrared data at high spatial and temporal resolution. J. Hydrometeorol. 5 (3), 487–503.

Kirstetter, P.E., Delrieu, G., Boudevillain, B., Obled, C., 2010. Toward an error model for radar quantitative precipitation estimation in the Cevennes-Vivarais region, France. J. Hydrol. 394 (1–2), 28–41.

Kirstetter, P.E., Viltard, N., Gosset, M., 2011. Building an error model for instantaneous satellite rainfall estimates. Quart. J. Royal Meterorol. Soc..

Kirstetter, P.E. et al., 2012. Toward a framework for systematic error modeling of spaceborne precipitation radar with NOAA/NSSL ground radar-based national mosaic QPE. J. Hydrometeorol..

Liang, X., 1994. A Two-Layer Variable Infiltration Capacity Land Surface Representation for General Circulation Models.

Negri, A.J., Adler, R.F., 1993. An intercomparison of three satellite infrared rainfall techniques over Japan and surrounding waters. J. Appl. Meteorol. 32 (2), 357–373.

Nicholson, S.E. et al., 2003. Validation of TRMM and other rainfall estimates with a high-density gauge dataset for West Africa. Part II: Validation of TRMM rainfall products. J. Appl. Meteorol. 42 (10), 1355–1368.

Ogden, F. et al., 2000. Hydrologic analysis of the Fort Collins, Colorado, flash flood of 1997. J. Hydrol. 228 (1), 82–100.

Qi, Y., Zhang, J., Zhang, P., 2012. A real-time automated convective and stratiform precipitation segregation algorithm in native radar coordinates. Quart. J. Royal Meterorol. Soc.. http://dx.doi.org/10.1002/qj.2095.

Sorooshian, S. et al., 2000. Evaluation of PERSIANN system satellite-based estimates of tropical rainfall. Bull. Am. Meteorol. Soc. 81 (9), 2035–2046.

Turk, F.J., Miller, S.D., 2005. Toward improved characterization of remotely sensed precipitation regimes with MODIS/AMSR-E blended data techniques. Geosci. Remote Sens. IEEE Trans. 43 (5), 1059–1069.

Tuttle, J.D., Carbone, R.E., Arkin, P.A., 2008. Comparison of ground-based radar and geosynchronous satellite climatologies of warm-season precipitation over the United States. J. Appl. Meteorol. Climatol. 47 (12), 3264–3270.

Vicente, G.A., Scofield, R.A., Menzel, W.P., 1998. The operational GOES infrared rainfall estimation technique. Bull. Am. Meteorol. Soc. 79 (9), 1883–1898.

Wang, J. et al., 2011. The coupled routing and excess storage (CREST) distributed hydrological model. Hydrol. Sci. J. 56 (1), 84–98.

Yong, B. et al., 2010. Hydrologic evaluation of multisatellite precipitation analysis standard precipitation products in basins beyond its inclined latitude band: a case study in Laohahe basin, China. Water Resour. Res. 46, W07542.

Zhang, X., 2012. Using NWP Analysis in Satellite Rainfall Estimation of Heavy Precipitation Events over Complex Terrain.

Zhang, J., Howard, K., Langston, C., Wang, S., Qin, Y., 2004. Three-and four-dimensional high resolution national radar mosiac. ERAD Proc..

Zhang, J. et al., 2011. National mosaic and multi-sensor QPE (NMQ) system: description, results, and future plans. Bull. Am. Meteorol. Soc. 92, 1321–1338.

Zhao, R.-J., 1992. The Xinanjiang model applied in China. J. Hydrol. 135 (1–4), 371–381.